

# Effects of Microstructural Evolution on the Thermal Conductivity of $\alpha$ -Al<sub>2</sub>O<sub>3</sub> Prepared from Nanosize $\gamma$ -Al<sub>2</sub>O<sub>3</sub> Powder

by

Eduardo J. Gonzalez, Grady White, and Lanhua Wei

Ceramics Division  
National Institute of Standards and Technology  
Gaithersburg, MD 20899

## Abstract

The thermal diffusivities ( $D$ ) of porous  $\alpha$ -Al<sub>2</sub>O<sub>3</sub> specimens prepared from nanosize  $\gamma$ -Al<sub>2</sub>O<sub>3</sub> powder and from conventional submicrometer-size alumina powders were measured at RT and the thermal conductivity ( $\kappa$ ) was calculated from  $D$ . Plots of  $\kappa$  vs the volume fraction of porosity ( $P$ ) showed that the data from both sets of samples followed similar linear curves. Similarly, data of Vickers hardness versus  $P$  obtained from the these same specimens also followed a single linear curve. The good correlation of thermal diffusivity with  $P$  suggests that grain boundaries have a lesser effect on thermal transport than porosity.

## I. Introduction

The thermal transport properties of polycrystalline dielectric materials are directly influenced by the materials microstructure. In dielectric materials, phonon propagation determines the transport of thermal energy. Microstructural features such as pores, grain boundaries, line defects and point defects scatter phonons, and, therefore, reduce the thermal conductivity ( $\kappa$ ). The influence of these features on  $\kappa$  is usually largest at low to moderate temperatures; at high temperatures multiphonon processes dominate. In most cases, the phonon scattering efficiency of each type of microstructural feature will show a different temperature dependence. For instance, scattering from point defects and impurities is most significant at room temperature, whereas scattering from surfaces and grain boundaries is most significant below room temperature [1]. Thus, it is useful to obtain a greater understanding of the interactions between microstructural features, such as porosity, which is ubiquitous in ceramic materials, and properties, such as thermal conductivity.

This work discusses the effects of randomly distributed porosity on the room temperature (300 K) thermal conductivity of  $\alpha$ -Al<sub>2</sub>O<sub>3</sub> prepared from nanosize powders and from conventional submicrometer-size powders. In particular, we have investigated the influence on  $\kappa$  of the very porous, vermicular microstructure that develops from the transformation of  $\gamma$ -Al<sub>2</sub>O<sub>3</sub> to  $\alpha$ -Al<sub>2</sub>O<sub>3</sub> during sintering of nanosize powders. This material was chosen because the vermicular microstructure is characterized by a homogeneous distribution of fine pores (pore dimensions  $\ll 1.0 \mu\text{m}$ ). Furthermore, this

vermicular microstructure is unique to  $\text{Al}_2\text{O}_3$  ceramic due to the creation of a continuous solid network of  $\alpha\text{-Al}_2\text{O}_3$  at the early stages of sintering. For comparison, thermal conductivity measurements were also made on specimens prepared from the conventional submicrometer-size  $\alpha\text{-Al}_2\text{O}_3$  powder. Finally, we measured the Vickers hardness of all of the specimens as a function of porosity. The Vickers hardness and the thermal conductivity both showed a linear dependence on porosity.

## II. Experimental Procedures

### (1) Sample Preparation and Characterization

The nanosize  $\gamma\text{-Al}_2\text{O}_3$  starting powder used in this work was Aluminum Oxide C (reported purity > 99.6 %), commercially available from Dugussa, AG, Geschäftsbereich Anorganische Chemieprodukt, Frankfurt, Germany. In an earlier study, the powder was found to consist primarily of  $\gamma$  phase with < 10 % by volume of  $\delta$  phase, as determined by transmission electron microscopy (TEM) and x-ray diffraction (XRD) techniques [2]. The powder was equiaxed with an average particle diameter of 20 nm. Samples of  $\alpha\text{-Al}_2\text{O}_3$  in the form of disks 3 mm in diameter by 0.5 mm thick, were prepared by cold compacting the  $\gamma\text{-Al}_2\text{O}_3$  nanosize powder in a WC-Co piston-cylinder apparatus at 1 GPa pressure. The high compaction pressure was needed to obtain structural integrity of the green bodies. The specific details of the compaction process and the apparatus are described elsewhere [3]. The density of the disks was calculated from the physical dimensions and the weight.

Specimens were also prepared by compacting high purity commercial  $\alpha\text{-Al}_2\text{O}_3$  powder of 0.3  $\mu\text{m}$  average particle size and average purity > 99.99 % (Sumitomo AKP-13, Japan). Pellets 2.0 cm in diameter and 0.5 cm in thickness were made by dry uniaxial compaction to 70 MPa, and subsequent cold isostatic compaction to 200 MPa. The density of the specimens was calculated from the physical dimensions and the weight of the pellets.

The specimens were divided into sets of three to five disks. Each set was sintered in air at 0.1 MPa (1 atm) pressure in a box furnace for 5 h at 1000 °C, 1100 °C, 1200 °C, 1300 °C, 1400 °C, 1500 °C, or 1600 °C. The porosity of the specimens was calculated using the mass and volume of the specimen and quantitative stereology.

The microstructure of the green bodies and the sintered samples was studied with a transmission electron microscope (TEM) and a scanning electron microscope (SEM). The mean intercept length technique was used to measure the grain size. X-ray diffraction was also used to monitor the transformation of  $\gamma\text{-Al}_2\text{O}_3$  to  $\alpha\text{-Al}_2\text{O}_3$ .

### (2) Thermal Diffusivity Measurements

The photothermal deflection technique was used to measure the thermal diffusivity (D) [4]. The technique uses an intensity-modulated argon-ion laser beam (4  $\mu\text{m}$  to 6  $\mu\text{m}$  in diameter) which is directed perpendicular to the surface of the sample. The modulated laser beam induces modulated heating of the sample surface which acts a source for

thermal waves that diffuse both into the sample and into the air adjacent to the surface of the sample. The thermal waves in the air are probed with a He-Ne laser beam reflected from the specimen surface at an angle less than  $5^\circ$  from the specimen surface. The reflected beam passes through the air just above the heated surface of the specimen. A quad-cell photodiode position-sensitive detector monitors the deflection of the probe beam that results from the passage of the beam through the thermally-induced index of refraction gradient in the air adjacent to the specimen. The probe beam deflection is measured as a function of the position of the probe beam relative to the heating beam, and the data are compared to the deflection calculated assuming 3-dimensional heat diffusion in a solid body [4-6]. Thermal diffusivity is obtained from a multiparameter least-squares-fitting procedure. The experimental uncertainty in  $D$  is  $<10\%$ , as determined from a calibration with high purity single crystal silicon having a known  $D$ .

We calculated  $\kappa$  from  $D$  using  $\kappa = D\rho C_p$ , where,  $\rho$  is the density of the specimen, and  $C_p$  is the specific heat of the specimen. ( $C_p$  for  $\alpha$ - $\text{Al}_2\text{O}_3 = 0.765 \text{ J/g} \cdot ^\circ\text{C}$  [8])

### III. Results

#### (1) Microstructure

The microstructures of the samples prepared from the  $\gamma$ - $\text{Al}_2\text{O}_3$  powder have been described in more detail previously [7]. Figure 1 shows a TEM micrograph of a compacted  $\gamma$ - $\text{Al}_2\text{O}_3$  green body. The particles have an equiaxed morphology with an estimated average dimension of 20 nm. Both XRD and electron diffraction results confirm that the grains are predominantly  $\gamma$  phase.

Figure 2 is a TEM micrograph of a sample sintered at  $1000^\circ\text{C}$ . The sample consists of a mixture of equiaxed particles of  $\gamma$  phase and isolated clusters of porous  $\alpha$  phase grains each approximately 250 nm in size. At this sintering temperature, necking between  $\gamma$  particles, indicative of partial sintering, was not observed. However, sintering of the porous  $\alpha$  phase grains was apparent and resulted in a spongy or vermicular structure with continuous porosity. The presence of  $\alpha$  and  $\gamma$  phases in these samples was confirmed with XRD analysis.

The samples sintered at  $1100^\circ\text{C}$  and higher were completely converted to the  $\alpha$  phase. These samples maintained the vermicular microstructure evidenced in the  $\alpha$ -phase of the specimen fired at  $1000^\circ\text{C}$ . Figure 3 shows the densification progress for samples sintered at: a)  $1100^\circ\text{C}$ , b)  $1200^\circ\text{C}$ , c)  $1300^\circ\text{C}$ , d)  $1400^\circ\text{C}$ , e)  $1500^\circ\text{C}$ , and f)  $1600^\circ\text{C}$ . Equiaxed  $\alpha$ -phase grains started to develop at the higher temperatures and pores disappeared progressively. The samples sintered at  $1500^\circ\text{C}$  and  $1600^\circ\text{C}$  had essentially the same bulk density. The grain size and pore size analysis for these samples is summarized in Table 1. It was impossible to measure the grain size of samples sintered between  $1100^\circ\text{C}$  and  $1300^\circ\text{C}$  because these samples did not exhibit a well defined grain morphology and grain boundaries were not easily identifiable.

To identify changes in porosity, a series of mercury porosimetry experiments were performed. Because the samples were small, limited information could be obtained. However, results from these experiments and from the microstructural observations suggest that both the solid phase and the porous phase were continuous throughout the samples sintered at 1100 °C and 1200 °C. Closed porosity and defined grain boundaries began to be identifiable at higher sintering temperatures. The densification progress as a function of sintering temperature is summarized in Fig. 4. Densification increases significantly with temperature between 1100 °C and 1400 °C and then asymptotes below full density. As described earlier, at 1500 °C and 1600 °C porosity trapped inside grains impedes further densification during the sintering times used for these experiments.

The densification progress of samples prepared with the  $\alpha$ -Al<sub>2</sub>O<sub>3</sub> sub-micron powder is also summarized in Fig. 4. Density increases systematically with sintering temperature to a maximum of 3.97 g·cm<sup>-3</sup>. Even though the specimens prepared from the different starting materials followed a similar densification curve, the microstructures that developed were very different. For example, after being sintered at 1100 °C, the samples prepared from the nanosize  $\gamma$ -Al<sub>2</sub>O<sub>3</sub> powder already formed a continuous solid network of  $\alpha$ -Al<sub>2</sub>O<sub>3</sub> phase material, whereas samples prepared from the submicrometer-size  $\alpha$ -phase powder maintained the appearance of a powder compact at the onset of neck formation between particles as seen in Fig. 5. However, both samples achieved approximately the same density after sintering at 1100 °C as seen in Fig. 4. There was no resolvable difference in density between the two type of samples sintered at 1500°C and 1600°C. The density of samples prepared with  $\gamma$ -Al<sub>2</sub>O<sub>3</sub> and sintered at 1600 °C (lowest fraction porosity) exhibited large scatter because these samples developed cracks more frequently during the sintering process. It is not known whether the cracks developed due to the transformation, due to the densification process, or due to local stresses generated during green body compaction.

## (2) Thermal Transport

A plot of room temperature thermal conductivity vs fractional porosity is shown in Fig. 6. The uncertainty bars in Fig. 6 (one standard deviation) were determined from normal error propagation procedures and the experimental scatter of the P and D measurements. Data for two of the samples are not shown in Fig. 6: the specimen with the pure  $\gamma$ -phase and the specimen with the mixed  $\gamma/\alpha$ -phase. Data from these specimens were excluded due to possible dependence of  $\kappa$  on the phase.

In order to estimate  $\kappa$  of fully dense  $\alpha$ -Al<sub>2</sub>O<sub>3</sub>, two straight lines were fitted to the data and extrapolated to P=0. The intercepts are  $(0.373 \pm 0.013) \text{ W} \cdot \text{cm}^{-1}\text{K}^{-1}$  for the nanosize starting material and  $(0.415 \pm 0.012) \text{ W} \cdot \text{cm}^{-1}\text{K}^{-1}$  for the submicrometer-size starting material. The uncertainties are the standard errors in the fit parameters. The slopes of the fitted lines differ by less than 1 %. The 10 % offset between the curves is most likely a result of differences in the purity of the powders used. Supporting this argument is the fact that the nanosize powder of  $\gamma$ -Al<sub>2</sub>O<sub>3</sub>, susceptible to impurity contamination due to its high surface area, exhibits lower  $\kappa$ . Our calculated values are somewhat higher than

typical values found in the literature:  $0.350 \text{ W} \cdot \text{cm}^{-1}\text{K}^{-1}$  at  $0 \text{ }^\circ\text{C}$  [9],  $0.3029 \text{ W} \cdot \text{cm}^{-1}\text{K}^{-1}$  at  $25 \text{ }^\circ\text{C}$  [10], and  $0.360 \text{ W/cm}^\circ\text{C}$  at  $28 \text{ }^\circ\text{C}$  [8]. One reason for the disagreement may be the differences in purity of the starting materials; in most cases the purity of the starting material was not reported in the literature. The higher  $\kappa$  values obtained in this work may be due to the higher purity of the powders used to prepare our specimens. The standard uncertainties in the literature values are not reported.

#### IV. Discussion

The strong effects of porosity on thermal transport have always been important for the preparation of thermal insulators and thermal conductors. Earlier work by Francl et al. [11] and Loeb [12] had shown significant effects of  $P$  on  $\kappa$ . Other authors have also developed model functions to predict the effect of porosity on general properties ( e.g. thermal conductivity, elastic modulus, etc. ) [11-16]. Most model functions are simple expressions that predict a linear or almost linear relationship between  $\kappa$  and  $P$  in dilute solutions of pores. In this context, a dilute solution is defined as a pore concentration for which the temperature field created around one pore does not interact with neighboring pores. Most models also assume non-contiguous spherical, isometric, or cylindrical pores. Francl et al. [11] showed that the relationship between the direction of heat flow relative to the orientation of cylindrical pores has a significant effect on  $\kappa$ , demonstrating that the important parameter is not necessarily  $P$  but rather the minimum Solid Area Fraction (SAF) in the direction of the heat flux. Consequently, the character of the porosity, e.g., shape, size, and relative orientation to the heat flux, is important in modeling thermal properties. Many expressions have been given that model only  $\kappa$  vs  $P$ ; thus, they do not take account of the minimum SAF. Clearly, the shape and orientation of the pores can affect the thermal conductivity and can also cause thermal conductivity anisotropy. Thus, samples of a given material with abundant elongated pores, may exhibit a different thermal conductivity than samples of the same material with spherical pores even though  $P$  may be the same in both specimens.

The porosity of the specimens studied here does not appear to exhibit any special morphology that could produce anisotropy in the thermal conductivity. The porosity in our specimens most likely has a random morphology, at least during the early stages of sintering. At later stages of the densification process, pores within grains typically approach a spherical shape, while pores at grain boundaries assume a lenticular shape. Due to the random orientation of the grain boundaries, the anisotropy of each lenticular shape is not expected to create anisotropy in the SAF. Thus, for our specimens  $P$  should provide a measure of the SAF, and as will be shown later, also  $\kappa$ . To verify this, quantitatively, stereology was conducted on polished sections of some of the specimens prepared from  $\gamma\text{-Al}_2\text{O}_3$ . In principle, the SAF determination done by point counting should be equivalent to  $P$  in specimens with spherical or randomly-oriented/randomly-shaped pores.

Indeed, results obtained from the alumina specimens in this work show good agreement between the SAF calculations from stereology and the  $P$  determinations from the physical

dimensions and weight of the specimens. (See Table 2.) Thus,  $P$  is proportional to the SAF in these specimens.

In a recent review of the influence of the porosity on physical properties, Rice [16] reiterated the significance of the percolation limit,  $P_c$ , which is a value of  $P$  above which a specific physical property (e.g., thermal conductivity, hardness, stiffness, etc.) is insensitive to further changes in relative density. At  $P > P_c$  particle-particle contact is insufficient to fully transmit physical forces. Following Rice [16], we calculate that  $P_c \approx 0.45$ . This number corresponds to an average relative density of 55% which is near the average relative density of a green body powder compact. This implies that the low thermal conductivity in green body compacts results primarily from the low SAF available for heat flow. Thus, it can be inferred that material linkage dominates room temperature heat flow in porous materials.

To pursue the idea that minimum SAF strongly influences the physical properties of porous materials, we have obtained Vickers hardness data from the same specimens used to obtain  $\kappa$ . It has been suggested that hardness is also controlled by particle-particle cross-sectional contact area [16]. The hardness results are shown in Figure 7. In this porosity range, the data from both sets of materials follow a common straight line. A linear extrapolation to  $P=0$  provides the approximate hardness of  $\approx 21$  GPa for a fully dense specimen. This value agrees well with average reported values for crystalline alumina ( $\approx 19$  GPa to 22 GPa) [17].

If we normalize the measured hardnesses by the hardness at zero porosity, and normalize the measured  $\kappa$  with  $\kappa$  at zero porosity, we find that all of the data fall on a common linear curve as seen in Fig. 8. These results strongly suggest that, as predicted, both properties appear to be controlled by the same microstructural characteristic, in this case,  $P$  and SAF. Accordingly, this also suggests that for a specimen with random shaped pores, a measurement of  $P$  is a good predictor of particle-particle contact area or minimum SAF. This conclusion is also supported by the data in Fig. 6. The two sets of specimens exhibited nearly the same relationship between  $\kappa$  and  $P$ , even though the different powders used in the specimen preparation produced specimens with different microstructures as described above. These results suggest that thermal resistance between particles or grains has a smaller effect on room temperature thermal conductivity than the lack of SAF normal to the heat flow direction. Similar observations have been made by Josell et al. [18] in thin film coatings consisting of 10, 20, and 40 bilayers of aluminum oxide and molybdenum. Their results suggest that the bulk properties of the individual layers are much more significant than the interface resistance between layers in determining the mean thermal conductivity of the composite coatings. Thus, the composition of the solid material and  $P$  are the dominant characteristics of the microstructure that limit room temperature thermal conduction in ceramic materials.

Based upon the results presented above, we have used a simple empirical equation proposed by Koh and Fortini [14] to describe  $\kappa$  vs  $P$ . Their expression can be written  $\kappa/\kappa_0 = (1-nP)$ , where  $P \ll 0.4$ ,  $\kappa_0$  is the thermal conductivity of the fully dense material, and

n is a fitting parameter. Typically,  $P \ll 0.3$  in alumina ceramics. For this work,  $n = 2.5$ , in good agreement with the value (2.1) found by Koh and Fortini [14] for samples with random porosity. The expression holds well in the case of alumina ceramic specimens that show randomly oriented pores with no characteristic morphology.

## **V. Conclusions**

The thermal conductivity of porous  $\alpha$ - $\text{Al}_2\text{O}_3$  specimens prepared from  $\alpha$ - $\text{Al}_2\text{O}_3$  submicrometer-size powder and  $\gamma$ - $\text{Al}_2\text{O}_3$  powder exhibited a linear dependence on porosity, where  $P \leq 0.45$ . Vickers hardness data obtained on these same specimens exhibited a similar linear relationship. The excellent correlation of these properties with  $P$  suggests that the thermal resistance across boundaries of partially sintered particles has a smaller influence on room temperature thermal conductivity than  $P$ . These results also indicate that for samples with randomly distributed pores,  $P$  can be directly correlated to the minimum SAF of the material in the specimen.

## References

\*Certain trade names and company products are mentioned in the text or identified in illustrations in order to adequately specify the experimental procedure and equipment used. In no case does such identification imply recommendation or endorsement by the National Institute of Standards and Technology, nor does it imply that the products are necessarily the best available for the purpose.

1. Thermal Conductivity of Solids, J. E. Parrott and Audrey D. Stuckes, Pion Limited, London.
2. M. R. Gallas, B. Hockey, A. Pechenik, and G. J. Piermarini, *J. Am. Ceram. Soc.*, **77** [8] 2107-12 (1994).
3. W. Chen, A. Pechenik, S. J. Dapkunas, G. J. Piermarini and S. G. Malghan, *J. Am. Ceram. Soc.*, **77** [4] 1005-1010 (1994).
4. P. K. Kuo, E. D. Sandler, L. D. Farvo, and R. L. Thomas, *Can. J. Phys.* **64**, 1168-1171 (1986).
5. L. Wei, Ph.D. Dissertation, Wayne State University, Detroit, MI (1992).
6. D. Josell, E. J. Gonzalez, and G. S. White, *J. Mater. Res.*, Vol. **13** [5] 1117-1119 (1998).
7. E. J. Gonzalez, B. Hockey, and G. J. Piermarini, *Materials and Manufacturing Processes* **11** [6], 951-967 (1996).
8. F. P. Incropera and DeWitt, Fundamentals of Heat Transfer, John Wiley & Sons, N.Y., (1981).
9. CRC Handbook of Chemistry and Physics 78th Edition, 1997-1998.
10. J. Francl and W. D. Kingery, *J. Am. Ceram. Soc.* **37** [2] 80-84 (1954).
11. J. Francl and W. D. Kingery, *J. Am. Ceram. Soc.* **37** [2] 99-107 (1954).
12. A. L. Loeb, *J. Am. Ceram. Soc.*, **37** [2] 96-99 (1954).
13. R. M. Spriggs, *J. Amer. Ceram. Soc.*, 628-629, Dec. 1961.
14. J. C. Y. Koh and A. Fortini, *Int. J. Heat Mass Transfer*, Vol. 16, 2013-2022, 1973.
15. F. P. Knudsen, *J. Am. Ceram. Soc.*, **42** [8] 376-387 (1959).
16. R. W. Rice, *J. Mater. Sci.*, **31** 102-118 (1996).
17. A. Krell and P. Blank, *J. Am. Ceram. Soc.* **78** [4] 1118-1120 (1995).
18. D. Josell, A. Cezairliyan, and J. E. Bonevich, *Inter. J. of Thermophysics*, **19** [2], 525-535 (1998).

Table 1. Mean Intercept Length Data

Sintering Temperature (°C)	Vol. Fraction Porosity, %	Grains Size* (μm) (±one standard deviation)	Pore Size* (μm)
1100	37.8	-----	continuous phase
1200	30.1	-----	0.168 ± 0.105
1300	21.1	-----	0.195 ± 0.096
1400	13.5	0.96 ± 0.123	0.44 ± 0.22
1500	< 5.4	1 - 3	< 1
1600	< 5.9	1 - 4	< 1

\* The grain size and pore values represent a mean intercept length.

Table 2. Comparison between volume fraction porosity calculated from physical dimensions and stereology.

Sintering Temperature (°C)	Vol. Fraction of Porosity (calculated from physical dimensions and weight ), %	Vol. Fraction of Porosity (determined by point counting), %
1200 °C	30.1 ± 1.0	28.6 ± 1.7
1300 °C	21.1 ± 0.7	23.8 ± 1.3
1400 °C	13.5 ± 0.5	13.2 ± 1.3

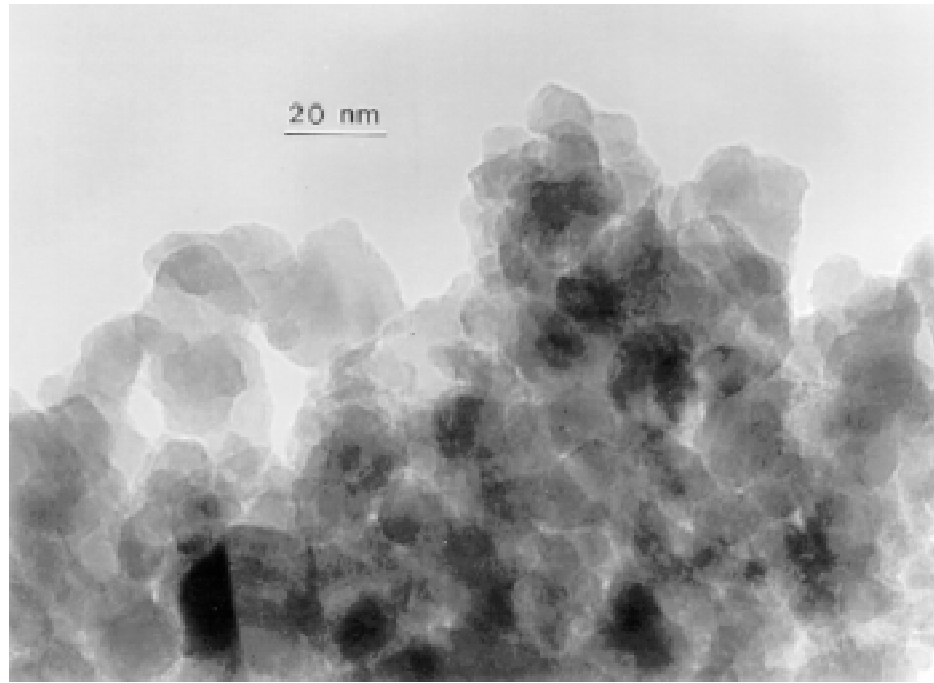


Figure 1. TEM brightfield image shows the microstructure of a green body compact of nanosize  $\gamma$ - $\text{Al}_2\text{O}_3$  powder pressed to 1 GPa in a piston/cylinder die.

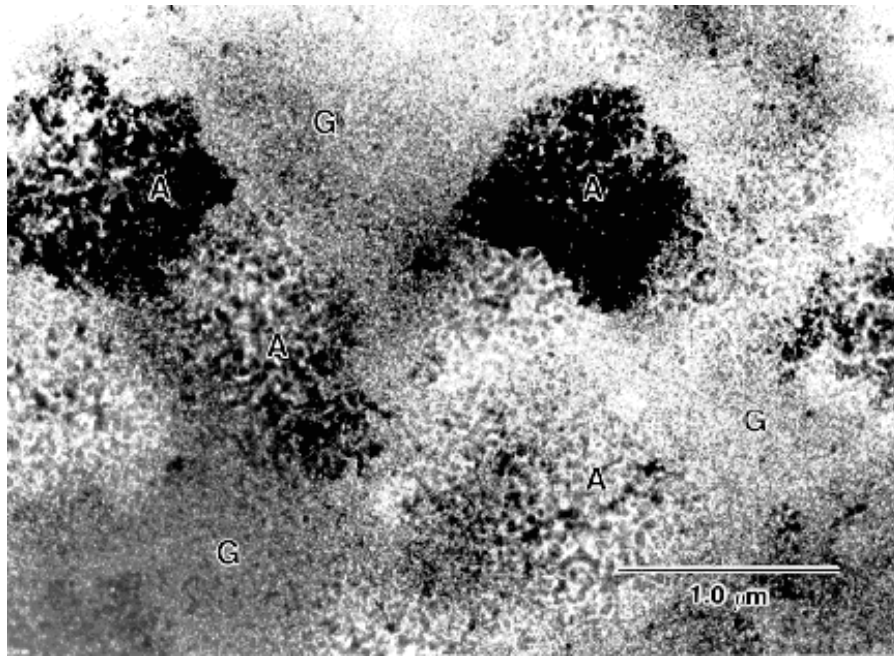


Figure 2. TEM brightfield image shows the microstructure of the sample shown in Figure 1 and sintered at 1000 °C for 5 h. The sample consists of a mixture of  $\gamma$ -phase particles (G) and isolated porous clusters of  $\alpha$ -phase alumina (A).

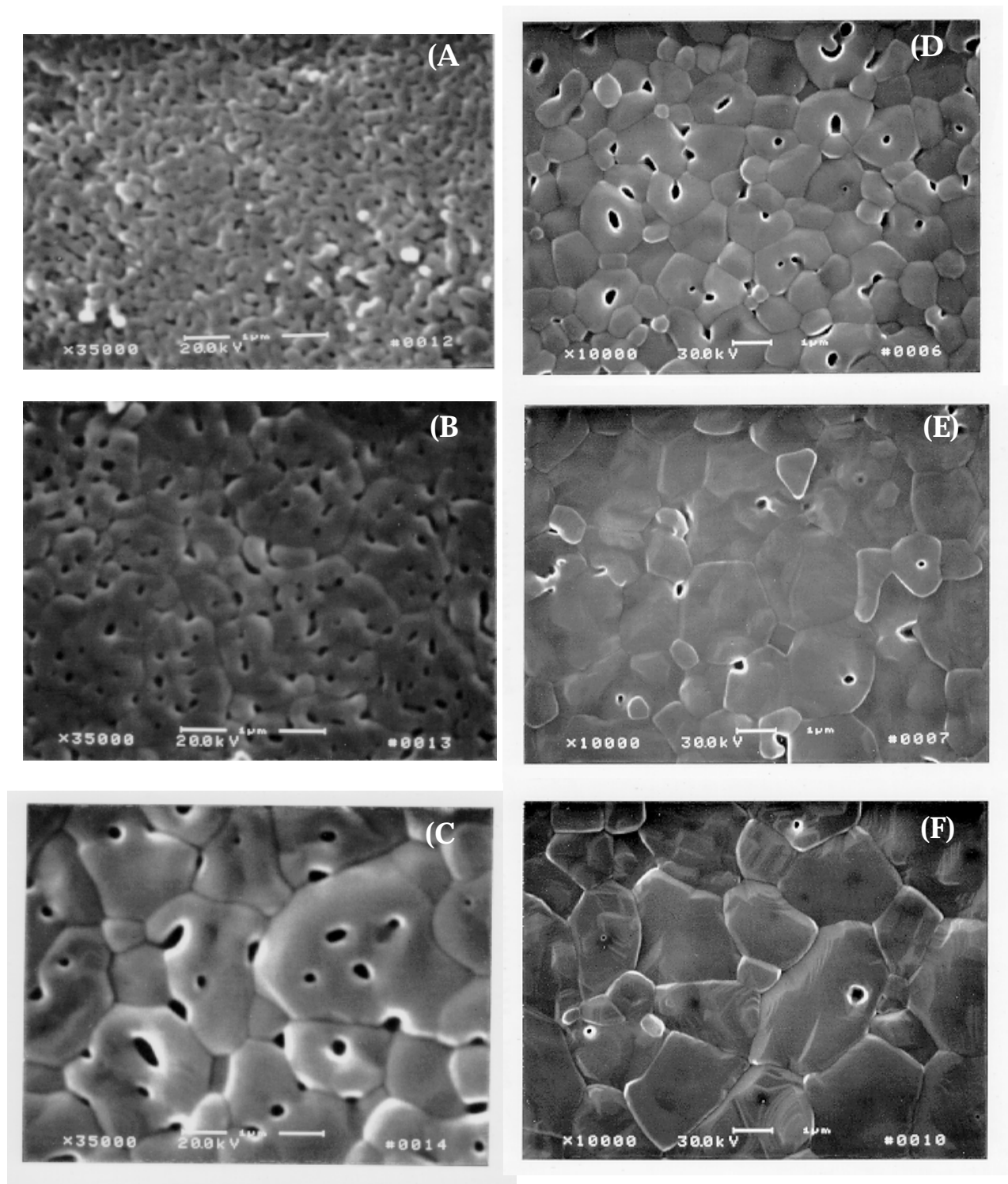


Figure 3A-F. SEM images show the microstructure development of  $\gamma$ - $\text{Al}_2\text{O}_3$  specimens pressureless sintered at (A) 1100 °C, (B) 1200 °C, (C) 1300 °C, (D) 1400 °C, (E) 1500 °C, or (F) 1600 °C for 5 h. All specimens have fully transformed to  $\alpha$ - $\text{Al}_2\text{O}_3$  at these sintering temperatures.

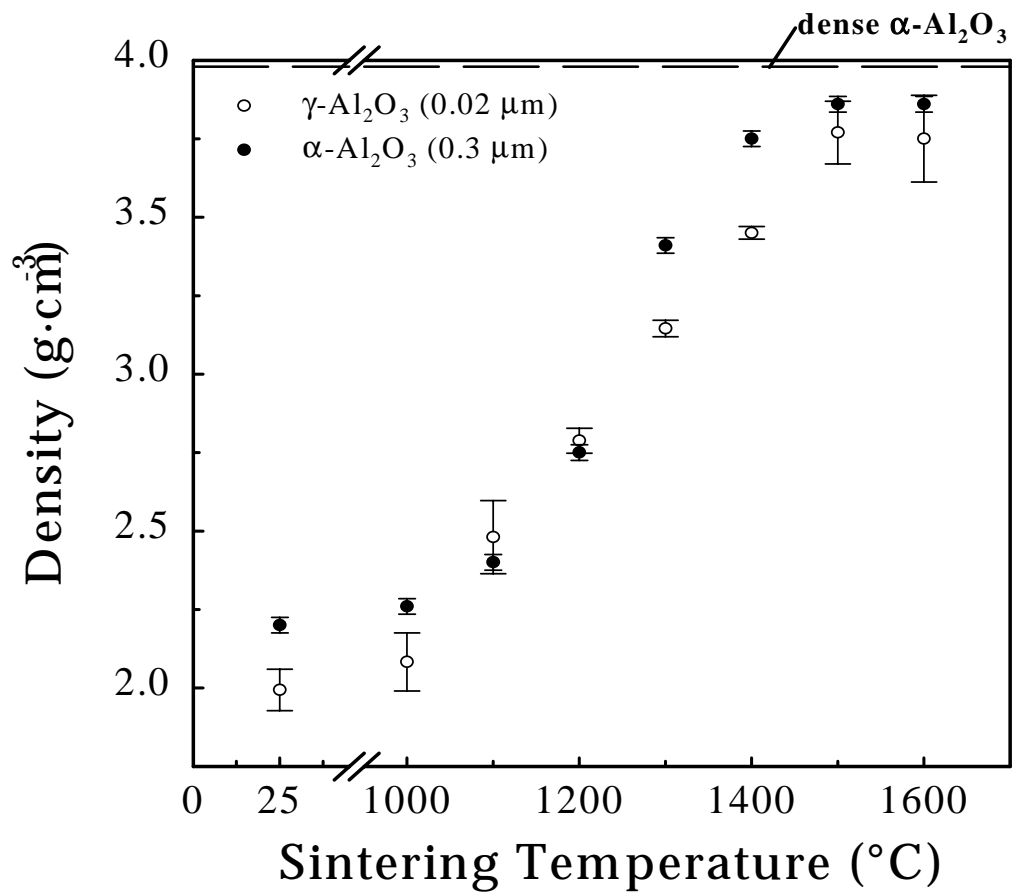


Figure 4. Bulk density of Al<sub>2</sub>O<sub>3</sub> compacts as a function of sintering temperature. Samples were sintered for 5 h.

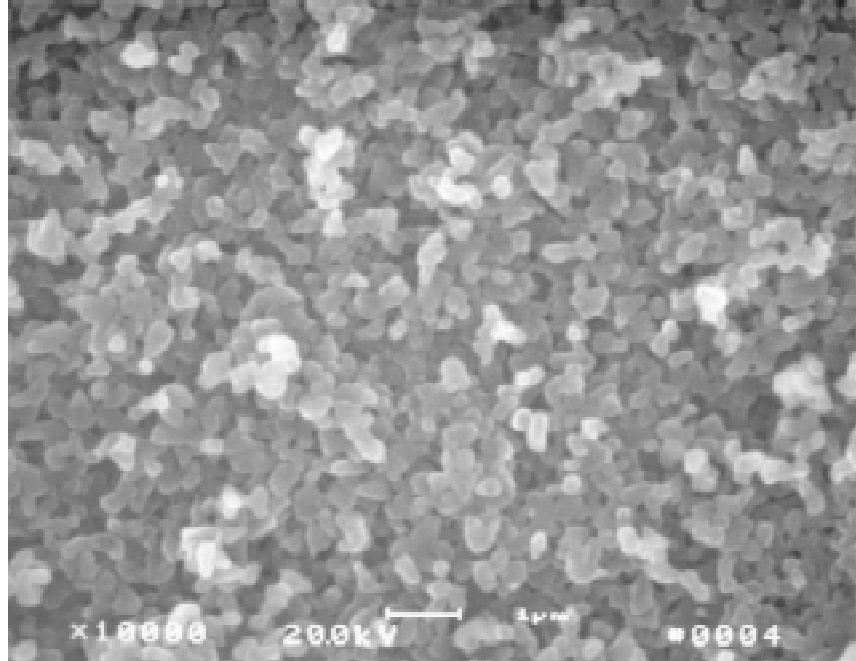


Figure 5. SEM image shows the microstructure of an  $\alpha$ -Al<sub>2</sub>O<sub>3</sub> powder compact prepared with sub-micron (0.3  $\mu$ m) powder and sintered at 1100 °C for 5 h.

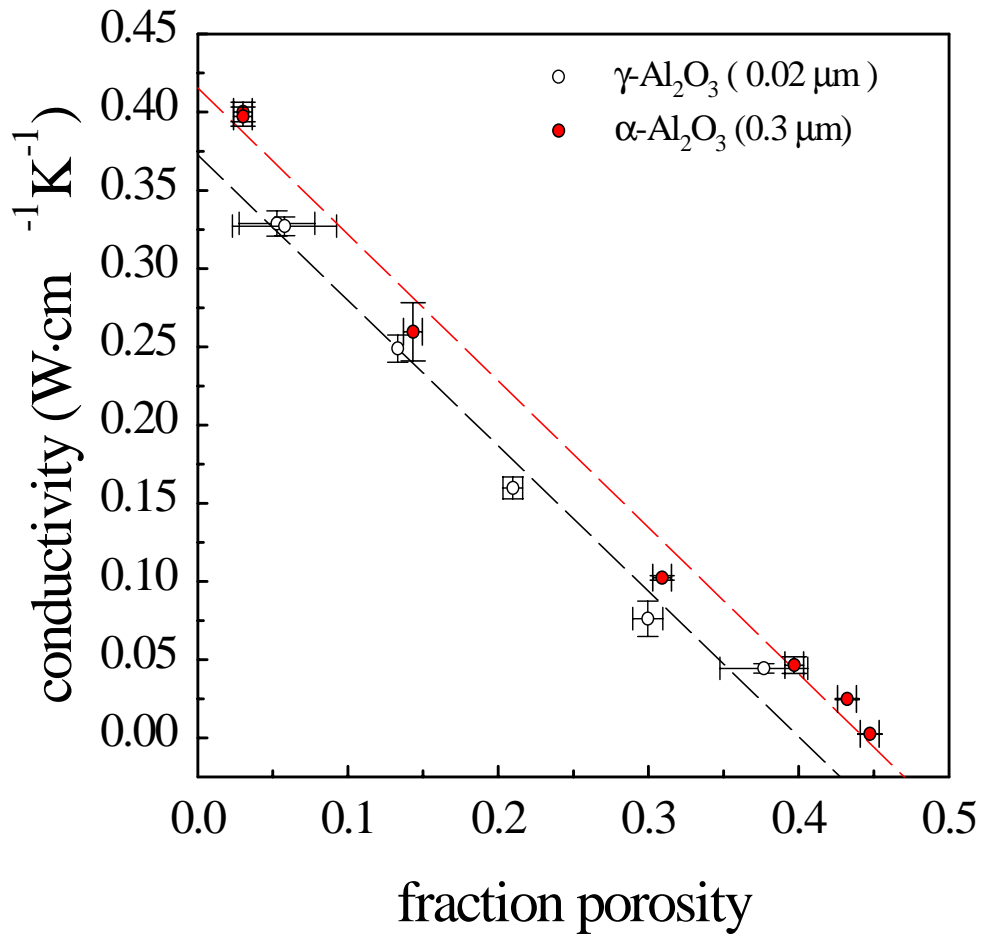


Figure 6. Plot shows the thermal conductivity dependence of  $\alpha$ -Al<sub>2</sub>O<sub>3</sub> specimens with volume fraction of porosity for samples prepared with sub-micron (0.3  $\mu$ m)  $\alpha$ -phase powder and  $\gamma$ -phase nanosize powders.

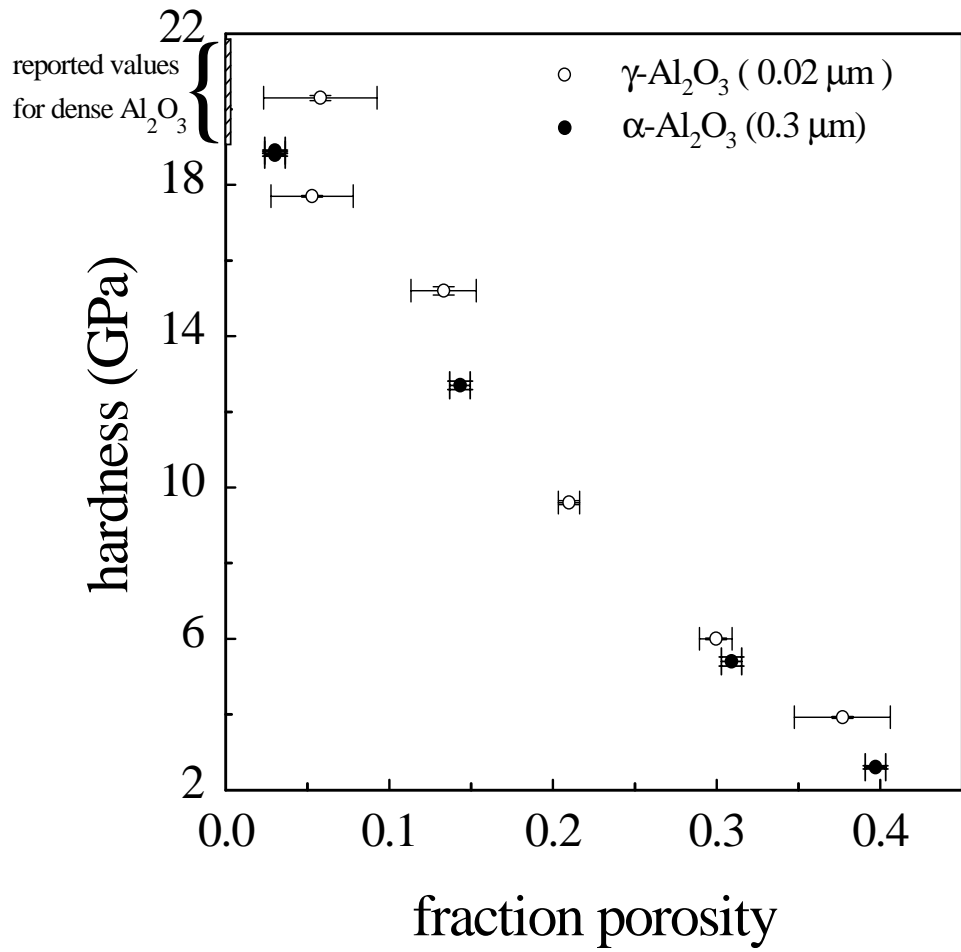


Figure 7. Plot shows Vickers hardness dependence of  $\alpha\text{-Al}_2\text{O}_3$  specimens with volume fraction of porosity for samples prepared with sub-micron (0.3  $\mu\text{m}$ )  $\alpha$ -phase powder and  $\gamma$ -phase nanosize powders.

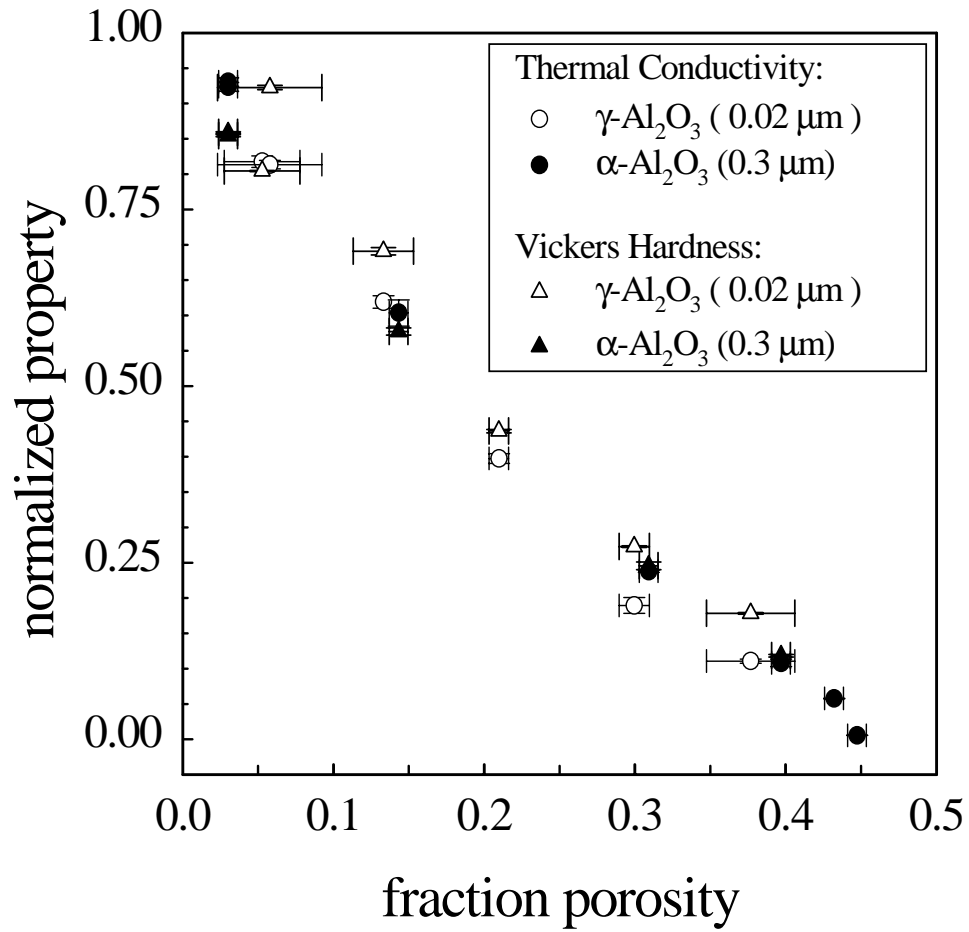


Figure 8. Comparison of thermal conductivity and hardness dependence with volume fraction porosity for samples of  $\alpha\text{-Al}_2\text{O}_3$  prepared with sub-micron (0.3  $\mu\text{m}$ )  $\alpha$ -phase powder and  $\gamma$ -phase nanosize powders.